ELSEVIER

Journal of Nuclear Materials 275 (1999) 268–276

journal of nuclear materials

www.elsevier.nl/locate/jnucmat

Mechanisms involved in thermal diffusion of rare earth elements in apatite

P. Martin[a,*], G. Carlot[a], A. Chevarier[a], C. Den-Auwer[b], G. Panczer[c]

[a] *Institut de Physique Nucléaire de Lyon, IN2P3-CNRS, 43 Bvd. du 11 Novembre 1918, F-69622 Villeurbanne cedex, France*
[b] *CEA/DCC/DRRV/SEMP, Marcoule, BP 171, F-30207 Bagnols-sur-Cèze, France*
[c] *Laboratoire de Physico-chimie des Materiaux luminescents, Université Claude Bernard Lyon 1, 43 Bvd. du 11 Novembre 1918, F-69622 Villeurbanne cedex, France*

Received 14 January 1999; accepted 21 May 1999

Abstract

In the context of radioactive waste disposal related to the back end of the nuclear fuel cycle, we study here the diffusion of lanthanide ions in hydroxyapatite. Two materials are considered as a possible migration barrier in the nuclear waste storage process. Lanthanum and europium have been chosen as representative elements of both fission products and actinide elements and were introduced in the apatite targets using ion implantation. The analysis of the evolution of profile distribution as a function of annealing conditions leads to low values of diffusion coefficients. A possible explanation is that the lanthanide ions substitute the calcium ions in the apatite structure and diffuse through these positions. Time-resolved laser induced luminescence measurements show that the europium ions substitute the calcium ions in both hydroxyapatite Ca(I) and Ca(II) sites. Probing the two sites has been performed by extended X-ray absorption fine structure (EXAFS) measurements in order to precise the europium environment.

1. Introduction

Apatites are potentially valuable materials to be used as migration barriers for nuclear wastes disposal in deep geological sites [1,2]. They could be introduced either in containers acting as a second migration barrier in high level waste storage or in concrete structures surrounding these containers (third migration barrier). In this context, data obtained from migration studies of uranium fission in core samples surrounding the Oklo fossil reactor are of primary importance. The measured yield of rare earth proved that the lanthanide ions remain bounded not only in uranyl grains, in clays, but also in newly crystallized minerals such as hydrothermal apatites [3,4]. The aim of this work is to obtain diffusion data and to understand the mechanisms involved in thermal diffusion of lanthanide in apatites. In this paper, lanthanum and europium have been chosen as representative elements of fission products ($A \sim 140$ u) and of actinides as the chemical properties of La^{3+} and Eu^{3+} are very similar to those of trivalent actinides. The choice of Eu^{3+} was dictated because of its luminescence properties. Its diffusion data were compared to the lanthanum ones, which mass ($A = 139$ u) is very close to those of the maximum fission product yield.

The general formula for apatite is $Ca_{10}(PO_4)_6X_2$, X being a fluorine, chlorine ion or an hydroxyl group. The crystal structure of apatite (space group $P6_{3/m}$) permits a wide range of cation and anion substitutions [5–7]. In particular the two calcium positions have distinct stereochemistries (Ca(I) with C_3 symmetry surrounded 9 oxygen and Ca(II) with C_s symmetry surrounded by 6 oxygen and 1 (OH^-) ion [8,9]) and are able to accommodate a variety of univalent, divalent, and trivalent cations as substituents. These minerals display a very good thermal and chemical stability as well as a very small solubility in water ($pK_s = 57.5$ at 25°C) [10]. In addition, after irradiation, defects are known to recover very quickly at a temperature as low as 60°C [11]. Moreover, the high sorption capacity for a number of

* Corresponding author.

0022-3115/99/$ - see front matter
PII: S0022-3115(99)00126-9

heavy elements such as actinides and lanthanides makes this material suitable for the retention of radioactive wastes.

The first part of this paper is devoted to the diffusion study of both lanthanum and europium ions in the apatite structure using Rutherford backscattering spectroscopy. Single crystals of fluorapatite were chosen as reference samples to study the migration in the apatite lattice, while hydroxyapatite is representative of polycrystalline apatite found in sedimentary area. In the second part laser induced luminescence spectroscopy and extended X-ray absorption fire structure (EXAFS) measurements have been performed in order to grab structural information around europium atoms after implantation and as function of annealing conditions.

2. Experimental

2.1. Characterization techniques

2.1.1. Rutherford backscattering spectroscopy (RBS)

Coupling of ion implantation and Rutherford backscattering spectroscopy (RBS) is used to study lanthanide ion diffusion in apatite. In previous works by Cherniak et al. [12] and Cherniak and Ryerson [13] such a procedure permits the measurement of small diffusion coefficients within relatively short annealing times.

The RBS analysis was performed at the van de Graaff accelerator (VDG) of the 'Institut de Physique Nucléaire de Lyon' (IPNL), using 1.5 MeV α-particles. The beam current was kept equal to 3 nA in order to minimize charging and pulse pile-up effects. The surface depth resolution was equal to 10 nm. It was damaged by straggling in case of in depth analysis (as example the resolution reaches 30 nm at a 100 nm depth). The sensitivity concerning lanthanide ion profiling stand around 0.01 at.% in hydroxyapatite. It was strongly worsened in case of fluorapatite because such a natural mineral contains cerium and other rare earths and high mass components at a level up to several 1000 ppm. These impurities produced a background intensity which interferes with lanthanum RBS spectra. To minimize interferences from heavy elements in the apatite lattice, a background spectrum was taken for each sample and subtracted from spectrum recorded from the implanted sample. Therefore, lanthanum profiling in the fluorapatite was limited to 100 nm depth.

2.1.2. Luminescence

The luminescence spectra were investigated under nitrogen UV laser (337 nm) excitations which delivers pulses of 10 ns duration and 0.1 cm spectral width. The pulse energy was maintained to about 10 mJ. The luminescence observed at the geometry of 90° was analyzed by the Lot-Oriel INSTASPEC 5 CCD detector enabling time-resolving spectra acquisition: delay times and strobe pulse duration between 20 ns and 9 ms, spectral detection range 350–900 nm (1200 channels, spectral resolution 0.5–1 nm, gratings with 300 and 600 lines/mm), detector by intensified CCD matrix. The system was combined with an optical microscope enabling spectra acquisition at a micrometer scale.

2.1.3. Extended X-ray absorption fine structure (EXAFS)

The EXAFS spectra were recorded at the DCI high energy ring of the LURE facility (Laboratoire pour l'Utilisation du Rayonnement Electromagnétique, Orsay, France), operating at 1.86 GeV with an average beam current of 300 mA. Energy calibration was performed at the Fe K edge at 7131.3 eV. Si (1 1 1) double crystal monochromator and air filled ionization chamber detector (I_0) were used. Higher harmonics reflections were rejected by detuning the monochromator crystals by 20–30%. As the europium implanted profile corresponds to about 600 nm depth, electron total yield detection [14] was performed in order to emphasize the surface observation compared to the bulk.

2.2. Sample preparation

Two types of apatite were studied: (i) Natural mineral centimetric-size single crystals from Durango (Mexico). They were cut perpendicular to the *c*-axis, polished and annealed in air at 500°C during 6 h to remove polishing damage. (ii) Synthetic microcrystalline hydroxyapatite (referenced as DNA grade Bio-gel HTP), stacked into pellets at 0.4 GPa. The high crystallinity was confirmed by X-ray diffraction. Observation by scanning electron microscopy shows regular crystal sizes (60×20 nm) with the typical prism shaped morphology of hydroxyapatite [15]. This structure implies a high density of grain boundaries with a size less than 10 nm.

The two lanthanide ions were implanted in both apatites: lanthanum in fluorapatite and hydroxyapatite, europium in hydroxyapatite.

Fluoro and hydroxyapatite were implanted with 100 keV La^+ ions using the isotope separator of the IPNL. In case of fluorapatite single crystals a tilt of few degrees of the target was applied in order to avoid channeling of La ions. For this energy the mean range R is about 40 nm. The nominal dose was 5×10^{15} ions/cm^2 corresponding to a maximum La concentration of 2.5 at.%. The beam current during implantation was typically 5 μA/cm^2.

Hydroxyapatite was implanted with 200 keV Eu^+ ions. For this energy the mean range R is about 60 nm. The nominal dose was 2.5×10^{16} ions/cm^2 corresponding to a maximum Eu concentration of 4.5 at.%. The beam current during implantation was 5 μA/cm^2.

2.3. Data treatments

2.3.1. Lanthanide diffusion

The evolution of the concentration profile of implanted species are deduced from RBS measurements [16] as a function of annealing time. The initial profiles of the as implanted samples are Gaussian distributions:

$$C(x,t=0)=\frac{N_{\mathrm{impl}}}{\sqrt{2\pi}\,\Delta R}\exp\left[-\frac{(x-R)^2}{2\,\Delta R^2}\right].$$

Here $C(x,t=0)$ is the initial ion concentration, x the distance from the implanted surface, N_{impl} the implanted ion dose, R the mean range of the La or Eu ions and ΔR the range straggling. In case of as implanted hydroxyapatite samples, the R (36 nm) and ΔR (9 nm) values deduced from RBS spectra fits are in good agreement with the values given by the TRIM code [17]. While in fluorapatite, due to remaining channeling effect, the measured R was equal to 50 nm. Further annealings were performed in air at temperatures between 100°C and 600°C and 800°C and 1000°C for hydroxyapatite and fluorapatite, respectively. An upper annealing limit was set at 600°C for hydroxyapatite since chemical decomposition occurs at higher temperatures. In case of fluorapatite no migration phenomena could be observed under 800°C which is there the lower limit. The annealing times were in the range from 15 min to 3 h. A broadening of the distributions occurs with increasing annealing time. Experimental data are interpreted on the basis of models derived from Fick's second law.

$$\frac{\partial C}{\partial t}=D\frac{\partial^2 C}{\partial x^2}+v\frac{\partial C}{\partial x},$$

where C is the concentration of the diffusing species, t the time, D the diffusion coefficient and the velocity v related to the driving forces f by the Nernst relation:

$$v=\frac{fD}{kT},$$

where k is the Boltzmann's constant. Such a driving force induces a shift of the whole distribution of diffusing species. It is important to notice that it does not modify the value of D.

The Fick's law is a parabolic partial differential equation with one space variable. This equation is applied to a semi-infinite medium and we consider no loss of diffusion species through the surface. An accumulation of lanthanide ions at the surface is observed, it leads to an increase of $C(0,t)$ concentration with annealing time. The boundary conditions assumed in our case are:

- At the sample surface: $\left(\frac{\partial C}{\partial x}\right)_{x=0}=0$.
- The medium is infinite in the positive x-direction: $C(\infty,t)=0$.

The initial condition is the 'as implanted' lanthanide distribution $(C(x,t=0),\ 0<x<\infty)$.

In order to solve the Fick's second law, we have used a numerical approach. This approach, based on finite differences method, is fully described in Ref. [18]. Our implementation is based on the NAG FORTRAN library routine [19]. The input parameters are the value of coefficient diffusion and the velocity which are adjusted to reproduce the evolution of lanthanide concentration as function of annealing conditions.

The evolution of ion distribution with annealing conditions is presented in Fig. 1 (a) and (b) in case of fluoro and hydroxy apatites, respectively. Due to the depth resolution, each point corresponds to a mean concentration value integrated over at least 10 nm. Consequently neither the concentration, nor the distribution slope can be determined right at the surface. One can notice that in fluorapatite an annealing temperature up to 800°C is necessary to obtain similar broadening as those observed in hydroxyapatite at 500°C. In the hydroxyapatite case, the La dose is constant within the experimental uncertainty, whatever the temperature and the annealing time are. In fluorapatite case, the integration over the lanthanum profile corresponding to 900°C annealing during 3 h is 10% lower than that of the

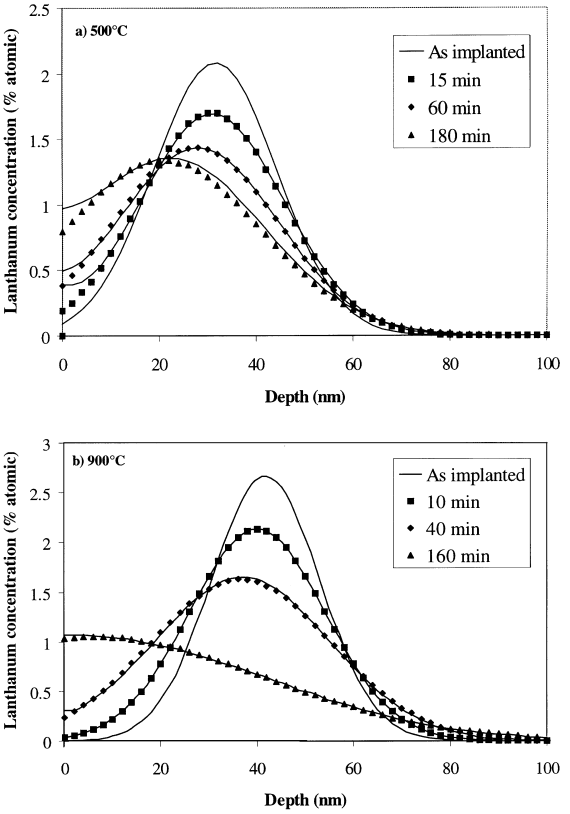

Fig. 1. Evolution of lanthanum profiles by RBS: (a) in hydroxyapatite 500°C; (b) in fluorapatite at 900°C versus annealing time. The diffusion fits are represented by lines.

implanted dose. This mismatch is due to limitation in the lanthanum profiling induced by the rare earth and heavy elements background as explained previously.

2.3.2. EXAFS

2.3.2.1. Data extraction. EXAFS oscillations are described by the general formula (1).

$$\chi(k) = \sum_{i=1}^{N} \frac{S_0^2}{kr_i^2} N_i |f_i(\theta, k, r_i)| \sin(2kr_i + \varphi_i(k) + 2.\delta_c(k)) \, e^{-2\sigma_i^2 k^2} e^{-2\pi/\lambda}, \quad (1)$$

where k is the momentum of the photoelectron defined by Eq. (2):

$$k = \sqrt{\frac{8\pi^2 m}{h^2}(h\nu - E_0)}. \quad (2)$$

Electronic parameters S_{0^2}, $f_i(v,k,r)$, $(\varphi_i k + 2\delta_c(k))$ and $\lambda(k)$ are related respectively to the electronic intrinsic losses, the backscattering amplitude of the i contribution, the backscattering phase of the i contribution and the electron mean free path. Structural parameters (N_i, r_i, σ_i) are respectively related to the number of neighbors, the absorbing atom to neighbor distance and the Debye–Waller factor for each i contribution.

The oscillations were extracted using EXAFS power code from Mikalowitch [20]. Linear extrapolation was used to remove background contribution and a five order polynomial function was used to model atomic absorption before Lengeler–Eisenberger normalization. Fourier transformation (FT) in k^3 was performed between 0.14 and 1.03 nm with Kaiser apodization window ($\tau = 2.5$). Inverse FT was carried out between 0.14 and 0.4 nm.

2.3.2.2. Fitting procedure. Phase shift, amplitude of the Backscattering wave function and λ were calculated using the FEFF702 simulation code from Zabinsky et al. [21] using apatite structure [22] at the Eu L_{III} edge, as fully described elsewhere [23]. Least square fitting of the experimental EXAFS oscillations were performed with 'Round Midnight' code from Mikalowitch [20] in the single scattering approximation. For all fits, S_0^2 was set to 1 and E_0 was set to 6983 eV.

3. Results

3.1. Diffusion

The diffusion coefficient values for lanthanum and europium in fluorapatite are 1.6×10^{-15} cm^2/s at 1000°C and 1.1×10^{-16} cm^2/s at 800°C. These results are in good agreement with the data obtained for lanthanum, samarium and lutetium in Ref. [24]. In hydroxyapatite similar diffusion coefficient values for europium and lanthanum are obtained and they are equal to 6×10^{-15} cm^2/s and 2.3×10^{-17} cm^2/s at 600°C and 400°C, respectively. The activation energies and pre-exponential factors deduced from the Arrhenius plot (Fig. 2) are 1.3 eV/at and 1.3×10^{-7} cm^2/s for hydroxyapatite and 2.1 eV/at and 5.1×10^{-7} cm^2/s for fluorapatite for lanthanide ions. A more rapid lanthanide ion diffusion in hydroxyapatite compared to the single crystal is observed (for example at 500°C: 4.4×10^{-16} cm^2/s to be compared with 6.2×10^{-21} cm^2/s). This is very likely due to the presence of grain boundaries which facilitate the diffusion process. Meanwhile, diffusion coefficients are found to be low compared to those obtained in other materials. It might explain the remarkable immobilization of lanthanide in the apatite lattice.

The order of magnitude of the velocity which induced a shift of the lanthanide distribution toward the surface are $10^{-4} < v < 10^{-2}$ nm/s in hydroxyapatite (temperature range 400–600°C) and $10^{-4} < v < 10^{-3}$ nm/s in fluroapatite (temperature range 800–1000°C). Because of the near surface implantation ($R_P \approx 40$ nm) and resolution profiling we could not afford accurate velocity v determination versus annealing temperature. Anyhow, the observation of the driving force together with the characterization of lanthanide substitution in the apatite lattice, will allow to propose a diffusion mechanism.

3.2. Microluminescence

It has been known for a long time that natural and synthetic apatites are fluorescent. By steady-state spectroscopy it was discovered that their luminescence is determined by characteristic bands of rare earth elements [8]. Trivalent europium ions are widely used as luminescent probes in the investigation of the crystallographic structure of the activator centers [8]. The

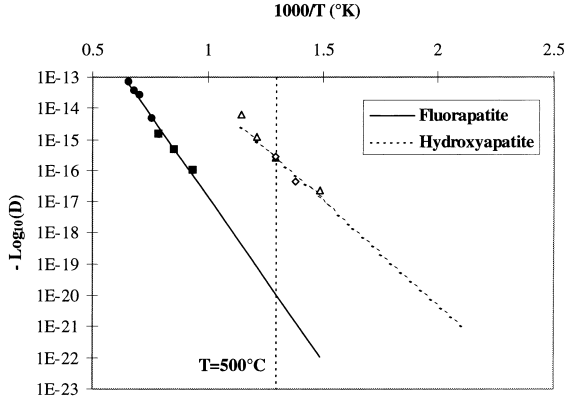

Fig. 2. Arrhenius diagram corresponding to hydroxyapatite and fluorapatite. Pre-exponential factors and activation energies are deduced from extrapolation (dashed and full lines).

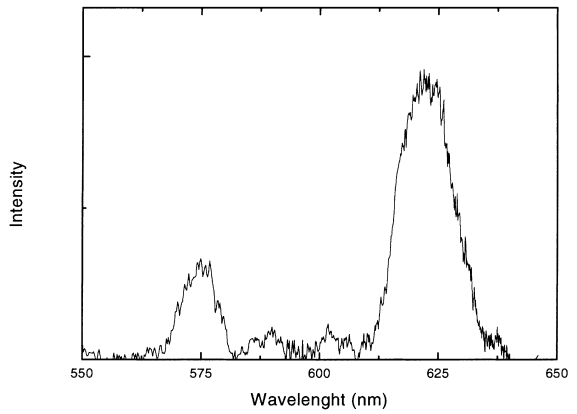

Fig. 3. Luminescence spectra (λ_{exc} 337 nm, delay: 500 ns, gate width: 5 ms) of as implanted apatite.

$^7F_0 \rightarrow {}^5D_0$ transition is particularly informative; as a matter of fact each Eu^{3+}center induces a specific emission line for this transition while the relative intensity is characteristic of the local symmetry [25].

The emission spectrum of the non-heated implanted pellet show very weak luminescent band (Fig. 3). The samples heated during 1 h at 400°C present an emission spectra with specific transitions of Eu^{3+} in Ca(I) sites corresponding to lines 621.5, 595 and 579 nm (Fig. 4). For longer annealing times, new bands appear at 630, 626 and 573.5 nm. Their intensity increases with time (2 and 3 h, Fig. 4) while previous line intensity decreases progressively. The same behavior is observed at 500°C and leads to complete disappearance of Ca(I) emission lines after annealing only for 2 h (Fig 4).

The first set of emission bands with the main one at 621 nm corresponds to the $^5D_0 \rightarrow {}^7F_2$ transitions of Eu^{3+} in high C_3 symmetry Ca(I) position while the second set with the main line at 573 nm corresponds to the same transitions of Eu^{3+} but in the low C_s symmetry Ca(II) position [26]. The weakness of the emission before any thermal induced diffusion indicates that the majority of the europium ions is not in a substitution position. However the energy of implantation allows the partial fixation of the europium ions inside the apatite lattice by substitution of Ca^{2+} in Ca(I) position. It is only in such crystallographic environment that the radiative transitions can occur. Providing thermal energy induces, as a function of time, diffusion of the europium ions and the substitution in Ca(II) sites. The oxidizing environment allows the charge compensation between Eu^{3+} and Ca^{2+}. At 400°C, the diffusion of Eu from Ca(I)

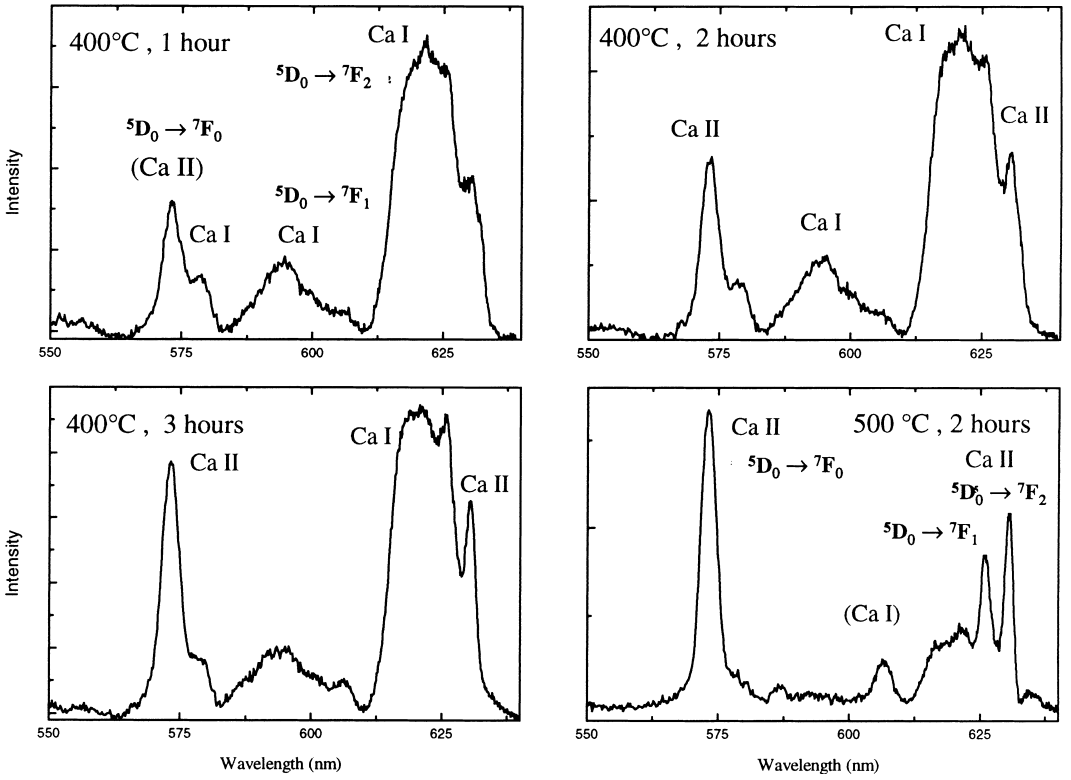

Fig. 4. Luminescence spectra (λ_{exc} 337 nm, delay: 500 ns, gate width: 5 ms) of thermally treated apatite (biorad) implanted with europium (5×10^{16} at/cm^2 at 200 keV).

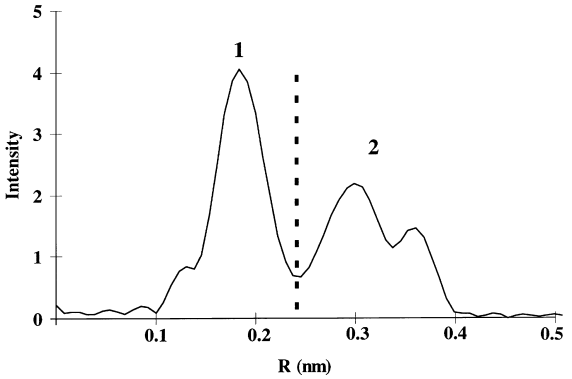

Fig. 5. Fourier transformation of k^3-weighted EXAFS spectrum for hydroxyapatite sample. Radial distribution functions were not corrected for phase shift. The two components are delimited by vertical dashed lines.

to Ca(II) sites occurs and over 500°C the complete migration to Ca(II) position is achieved.

3.3. EXAFS

3.3.1. Analysis of EXAFS spectrum of pure hydroxyapatite at the Ca K edge

Hydroxyapatite has a rather complex crystal structure in which the unit cell contains 2 $Ca_{10}(PO_4)_6(OH)_2$ units. Furthermore 4 calcium ions occupy the Ca(I) site and 6 occupy the Ca(II) site. Such a structure corresponds to a wide range of distances between the calcium and the oxygen atoms and leads to an extremely complex averaged EXAFS spectrum. In order to simplify, we consider average distances of oxygen shells.

To valid the fitting parameters to be used when the europium ions substitute the calcium ions in both Ca(I) and Ca(II) sites, the EXAFS spectrum of free hydroxyapatite has been fitted. Fourier transform of the experimental spectrum at the CA K edge is given in Fig. 5 and exhibits two regions (1 and 2) that were fitted using FEFF7.02 phases and amplitudes from the apatite

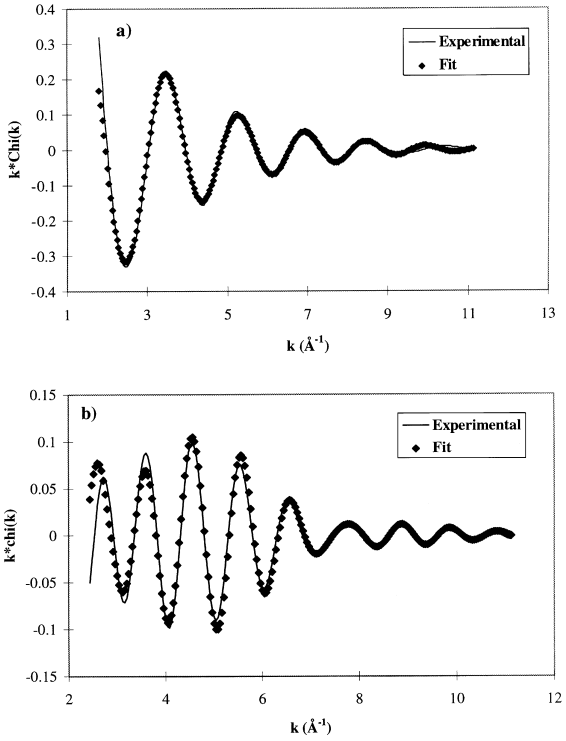

Fig. 6. Fourier-filtered first (a) and second (b) component to EXAFS for fitted with FEFF7 code calculation.

crystallographic structure [22]. Best fit parameters are given in Table 1 and compare well with the crystallographic data. Furthermore, these results are backed by those obtained by Harries et al. [27]. The fitting procedure and parameters used here are thus validated and will be used for europium implanted apatite. (See Fig. 6.)

3.3.2. Analysis of EXAFS spectrum of implanted hydroxyapatite at the europium L_{III} edge

As the luminescence study emphasizes the high probability of substitution in Ca(II) site after 2-h annealing at 500°C, we performed EXAFS measurements

Table 1
Average calcium environment for hydroxyapatite as determined by X-ray crystallography and EXAFS (N = number of neighbors, R = distance, σ = Debye–Waller factor)

		N	R (nm) EXAFS	R (nm) X-Ray [15]	σ (nm)
Region 1	Ca–O	6.6	0.241 ± 0.0005	0.242	0.0099 ± 0.0005
	Ca–O	1.8	0.273 ± 0.0005	0.275	0.0100 ± 0.0005
	Ca–P	2.4	0.320 ± 0.0001	0.320	0.0136 ± 0.0002
Region 2	Ca–Ca	0.8	0.345 ± 0.0001	0.344	0.0075 ± 0.0002
	Ca–P	3	0.360 ± 0.0001	0.360	0.0134 ± 0.0002
	Ca–Ca	6	0.406 ± 0.002	0.406	0.0137 ± 0.0002
			r factor $= 2.42 \times 10^{-2}$		

Table 2
Best fit EXAFS parameters corresponding to 4-hours annealing at 500°C (N = number of neighbors, R = distance, σ = Debye–Waller factor)

	N	R (nm)	σ (nm)
Eu–O	6.80 ± 0.09	0.241 ± 0.0004	0.0099 ± 0.0001
Eu–O	1.40 ± 0.01	0.273 ± 0.001	0.0100 ± 0.003
Eu–P	2.20 ± 0.02	0.319 ± 0.0002	0.0136 ± 0.001
	r factor $= 4.80 \times 10^{-2}$		

Table 3
Best fit EXAFS parameters corresponding to 3-hours annealing at 500°C (N = number of neighbors, R = distance, σ = Debye–Waller factor)

	N	R (nm)	σ (nm)
Eu–O	6.80 ± 0.09	0.241 ± 0.0004	0.0099 ± 0.0001
Eu–O	1.20 ± 0.01	0.273 ± 0.001	0.0100 ± 0.003
Eu–P	2.20 ± 0.02	0.319 ± 0.0002	0.0136 ± 0.001
	r factor $= 5.70 \times 10^{-2}$		

after the same annealing conditions to precise the Eu environment. Prior to any EXAFS data analysis we supposed that all the europium ions were in Ca(I) or Ca(II) substitution sites. Such an approximation is backed by the relativity high annealing temperature set point that ensures major migration of Eu^{3+}into Ca(II) sites, as suggested by the fluorescence measurements. Furthermore, the atomic concentration of implanted europium is strictly inferior to the doping limit of hydroxyapatite (5%) [7].

In order to simulate the Ca(II)/Ca(I) substitution ratio we performed several FEFF7.02 simulations at the Eu L_{III} edge. Resulting Fourier transforms are given in Fig. 7 and correspond to parameter evolution as shown in Fig. 8(a) and (b).

Best fit parameters given in Tables 2 and 3 correspond to the adjustment of the experimental EXAFS

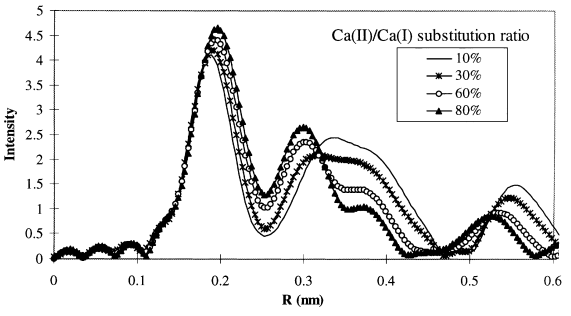

Fig. 7. Fourier transform of EXAFS spectra obtained by FEFF7.02 as function Ca(II)/Ca(I) substitution ratio.

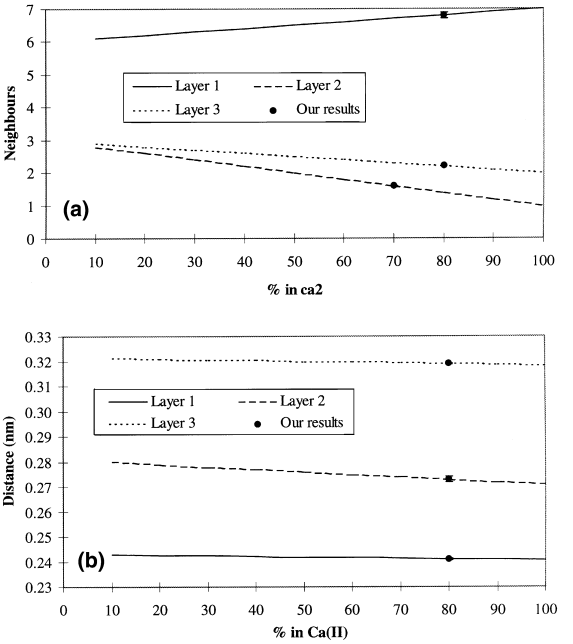

Fig. 8. Evolution of: (a) neighbors number; (b) distances as function Ca(II)/Ca(I) substitution ratio.

spectra corresponding to 500°C annealing for 4 and 3 h. The fit is represented in Fig. 9. Comparison with Fig. 8(a) and (b) suggest that 80% of Eu^{3+} are substituted to Ca(II) sites after 3 h and this percentage remains the same after 4 h. These values are very similar and no strong evolution after 3 h annealing is observed.

4. Discussion

Both luminescence and EXAFS data suggest that rate of lanthanide ions substituted to the calcium sites in the apatite structure increases with annealing times. Furthermore, the substitution ratio Ca(II)/Ca(I) in-

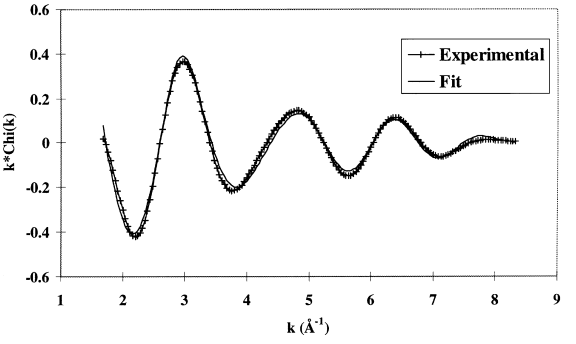

Fig. 9. Fourier-filtered to EXAFS for fitted with FEFF7 code calculation.

creases. After 3 h at 500°C for instance, about 80% of europium ions are located in the Ca(II) site. These results are in agreement with the site occupation ratio Ca(II)/Ca(I) ~ 4 determined by Fleet and Pan [6] in case of lanthanum doped synthetic fluorapatite crystals. In that case, charge compensation occurs because of the divalent and trivalent states of calcium and europium, respectively. We propose here a simple substitution mechanism that implies the contribution of other species. In our experimental conditions (annealing under air), substitution of trivalent lanthanide ions in hydroxyapatite could be compensated as follows:

Mechanism 1: substitution of OH^- by O^{2-}

$$Eu^{3+} + O^{2-} \leftrightarrow Ca^{2+} + OH^- \quad Ca_{10-x}Eu_x(PO_4)_6(OH)_{2-x}O_x.$$

It must be noted that the Ca(II) position is located near the OH^- lattice columns, and this could increase the probability of such a mechanism as far as oxygen diffusion through these columns is possible.

Mechanism 2: substitution of Ca^{2+} by a vacancy (Θ)

$$2Eu^{3+} + \Theta \leftrightarrow 3Ca^{2+} \quad Ca_{10-3x}Eu_{2x}\Theta_x(PO_4)_6(OH)_2.$$

Let us now connect these results to diffusion data. In case of both single crystal and polycrystalline apatite we can notice a slight shift to the lanthanide ions distribution toward the surface. In order to model the evolution of lanthanide atomic concentration profiles, a velocity connected to a driving force has to be introduced in the second Fick's Law. The challenge is to understand the physical meaning of this driving force.

One possible explanation to the lanthanide migration towards the surface could be the influence of defects created by implantation process. Indeed, the major annihilation process for defects is known to be their diffusion to the sample surface [28]. However, such an assumption has to be precluded because at annealing temperature larger than 400°C the defects recover very quickly (few seconds) [11]. Therefore, no influence on the diffusion process is to be attributed to defects.

The alternative is to connect the lanthanide distribution shift to Mechanism 1. In order to achieve charge compensation for all the lanthanide ions introduced in the samples a large amount of oxygen is needed (4 at.%). The only oxygen supply is provided by oxygen diffusion from the surface. Oxygen diffusion in fluoarapatite from the surface has been studied by Farver and Giletti [29]. They determined a diffusion coefficient at 800°C which stands between 3×10^{-15} cm^2/s for a 200 bar pressure and 1×10^{-14} cm^2/s for a 2000 bar pressure. Extrapolation of these data to our experimental conditions leads to a diffusion coefficient value around 10^{-17} cm^2/s which corresponds to a slower process than the one we observed here. In our system an oxygen concentration gradient appears from the surface to the bulk and generates a chemical potential. This potential leads to the preferential flux of lanthanide to the surface in order to obey charge compensation. This assesses that Mechanism 1 is the dominant process for diffusion under air. Meanwhile, Mechanism 1 is also backed by the fact that in case of rare earth diffusion under vacuum only substitution in Ca(I) is observed [26].

In this work, we conclude that the preferential mechanism in lanthanide divalent ion migration under air leads to substitution to Ca(II) site in apatite lattice. The increase in luminescence signal intensity from as implanted samples to annealed one together with diffusion data argues for the following process. After implantation most of the europium ions are not in substitution position and during annealing the europium diffusion is correlated to substitution process. This explains the low diffusion coefficients that were observed (i.e. 3×10^{-25} cm^2/s for hydroxypatite at 100°C). Such results are speaking in favor of apatites as filling materials in geological disposal. However, we must be aware that slight migration of lanthanide toward the surface has been observed and this could potentially make this material more easily damaged by water lixiviation.

Acknowledgements

The authors would like to thank N. Chevarier and N. Moncoffre for many helpful discussions. They would also like to thank A. Plantier and the accelerator team for providing the technical support.

References

[1] R.C. Ewing, W.J. Weber, F.W. Clinard Jr., Prog. Nucl. Energy 29 (1995) 63.
[2] R. Gauglitz, M. Holterdorf, W. Franke, G. Marx, Radiochim. Acta 58&59 (1992) 253.
[3] F. Gauthier-Lafaye, P. Holliger, P.P. Blanc, Geochim. Cosmochim. Acta 60 (1996) 4831.
[4] P.L. Blanc, F. Gauthier-Lafaye, P. Holliger, A. Winberg, E. Ledoux, I. Gurban, CEA-IPSN Report (1995) F12W-CT91-0071.
[5] E. Fleet, Y. Pan, J. Solid State Chem. 112 (1994) 78.
[6] M.E. Fleet, Y. Pan, Am. Mineral. 80 (1995) 329.
[7] M. Mikou, A. Taitai, J.L. Lacout, Ann. Chim Fr. 10 (1985) 645.
[8] R. Jagannathan, M. Kottaisamy, J. Phys.: Condens. Matter 7 (1995) 8453.
[9] R. Knubovets, Rev. Chem. Eng. 9 (1993) 161.
[10] S. Chander, D.W. Fuerstenau, in: D.N. Misra (Ed.), Solubility and Interfacial Properties of Hydroxyapatite: A Review, Plenum, New York, 1984.
[11] F. Villa, thesis, Université de Franche Comté, 1997.

[12] D.J. Cherniak, W.A. Lanford, F.J. Ryerson, Geochim. Cosmochim. Acta 55 (1991) 1663.
[13] D.J. Cherniak, F.J. Ryerson, Geochim. Cosmochim. Acta 57 (1993) 4653.
[14] J. Mimault, J.J. Faix, T. Girardeau, M. Jaouen, G. Tourillon, Meas. Sci. Technol. 5 (1994) 484.
[15] A. Ebrahimpour, M. Johnsson, C.F. Richardson, G.H. Nancollas, J. Colloid Interf. Sci. 159 (1993) 158.
[16] N. Moncoffre, G. Barbier, E. Leblond, P. Martin, H. Jaffrezic, Nucl. Instrum. and Meth. B 140 (1998) 402.
[17] J.P. Biersack, L.G. Haggmark, Nucl. Instrum. and Meth. 174 (1980) 257.
[18] J. Crank, The Mathematics of Diffusion, 2nd ed., Claredon, Oxford, 1975.
[19] NAGLIB Manual-FORTRAN, Mark 18, Vol. 2 D03PCF, 1997.
[20] A. Michalowicz, Soc. Franç. Chim. 116 (1991) 45.
[21] S.I. Zabinsky, J.J. Rher, A. Ankudinov, R.C. Albers, M.J. Eller, Phys. Rev. B 52 (1995) 2995.
[22] M.I. Kay, R.A. Young, Nature 204 (1964) 1050.
[23] P. Martin, thesis, University Lyon l, 1999.
[24] E.B. Watson, T.M. Harrison, F.M. Ryerson, Geochim. Cosmochim. Acta 49 (1985) 1813.
[25] M. Kottaisamy, R. Jagannathan, P. Jeyagopal, R.P. Rao, R.L. Narayan, J. Phys. D 27 (1994) 2210.
[26] M. Gaft, R. Reisfeld, G. Panczer, S. Shoval, B. Champagnon, G. Boulon, J. Lumin. 72–74 (1997) 572.
[27] J.E. Harries, D.W.L. Kukins, S.S. Hasnain, J. Phys. C 19 (1986) 6859.
[28] E. Bertel, W. Ritter, E. Bertagnolli, T.D. Mark, Phys. Rev. B 27 (1983) 3730.
[29] J.R. Farver, B.J. Giletti, Geochim. Cosmochim. Acta 53 (1989) 1621.